How to turn off a lava lake? A petrological investigation of the 2018 intra-caldera and submarine eruptions of Ambrym volcano

Yves Moussallam, Etienne Médard, Guillaume Georgeais, Estelle Rose-Koga, Kenneth Koga, Bernard Pelletier, Philipson Bani, Tara Shreve, Raphael Grandin, Marie Boichu, et al.

How to turn off a lava lake? A petrological investigation of the 2018 intra-caldera and submarine eruptions of Ambrym volcano.

Yves Moussallam[1,2*], Etienne Médard[3], Guillaume Georgeais[3], Estelle F. Rose-Koga[3], Kenneth T. Koga[3], Bernard Pelletier[4], Philipson Bani[3], Tara L. Shreve[5], Raphael Grandin[5], Marie Boichu[6,7], Dan Tari[8], Nial Peters[9]

[1] *Lamont-Doherty Earth Observatory, Columbia University, New York, USA*

[2] *American Museum of Natural History, Department of Earth and Planetary Sciences, NY 10024, New York, USA*

[3] *Université Clermont Auvergne, CNRS, IRD, OPGC, Laboratoire Magmas et Volcans, F-63000 Clermont-Ferrand, France*

[4] *Institut de Recherche pour le Développement (IRD), Antenne de Nouméa, Nouvelle Calédonie*

[5] *Institut de Physique du Globe (IPGP), Université de Paris, France*

[6] *Univ. Lille, UMR 8518 - LOA - Laboratoire d'Optique Atmosphérique, F-59000 Lille, France*

[7] *CNRS, UMR 8518, F-59000 Lille, France*

[8] *Vanuatu Meteorology and Geohazards Department (VMGD), Vanuatu*

[9] *University College London, London, United Kingdom*

Corresponding author: Yves Moussallam; yves.moussallam@ldeo.columbia.edu

Keywords: magma mixing; magma mingling; caldera subsidence; melt inclusion; basaltic eruption; geo-speedometer

ABSTRACT

In December 2018, an unusually large intra- and extra-caldera eruption took place at Ambrym volcano (Vanuatu). The eruption drained the volcano's five active lava lakes and terminated, at least momentarily, the surface activity that had been ongoing for decades to hundreds of years, sustaining the largest recorded persistent degassing on the planet. Here, we investigate the mechanisms and dynamics of this major eruption. We use major elements and volatiles in olivine and clinopyroxene hosted melt inclusions, embayments, crystals and matrix glasses together with clinopyroxene geobarometry as well as olivine and clinopyroxene geothermometry and diffusion modelling in crystals and embayments to reconstruct the chronology and timing of the subsurface processes that accompanied the eruption. We find that the eruption began with the meeting, mingling and limited chemical mixing of mostly two magma bodies occupying similar vertical but different horizontal locations in the crust, one corresponding to the main plumbing system at Ambrym that fed the lava lakes and the other corresponding to an older, previously cut-off and more chemically evolved branch of the plumbing system. Within the primitive magma, two texturally distinct components – one microlite-rich and one microlite-poor – can further be identified. The 2018 eruption hence provides a detailed image of Ambrym's complex plumbing system. Our diffusion timescales and geobarometric estimates coincide closely with geophysical observations. They point to a reconnection of the evolved magmatic branch with the main system occurring less than 10 h prior to the intra-caldera eruption and a period of two days for the subsequent >30 km lateral magma transport along a deeper dike prior to submarine eruption just off the SE coast of the island with the more primitive magma reaching first followed by mingled magma containing both compositions. Magma ascent rates is estimated at 95±24 m/s in the last ~2.5 km of ascent during the intra-caldera eruption and at 80±6 m/s in the last ~4 km of ascent during the submarine eruption. Comparison with other lava-lake-draining eruptions reveal striking

similarities both in terms of precursory activity, with lake level rising prior to eruption in all cases, and in term of plumbing system organisation with the presence of peripheral magma pockets, isolated from the main magmatic system but that can be mobilized and erupted when met by dikes propagating laterally from the main system.

INTRODUCTION

Lava lakes are the emblem of persistent degassing volcanic activity. They are rare examples of volcanic systems having reached a metastable equilibrium whereby gas and magma motions result in conduit dynamics allowing for efficient gas release whilst maintaining molten magma from the chamber to the surface (e.g., Tazieff 1994; Harris et al. 2005; Witham and Llewellin 2006; Harris 2008; Oppenheimer et al. 2009; Burgi et al. 2014; Moussallam et al. 2015a, 2016; Allard et al. 2016b). As a result, volcanoes with lava lakes tend to rank amongst the major emitters of volcanic gases to the atmosphere – at least for the past decade (Carn et al. 2017) – and to maintain surficial activity that can remain nearly unchanged for decades to centuries. In 2018 two of the most iconic lava lake volcanoes, Kīlauea and Ambrym, both experienced major eruptions whereby subsurface magma migration, associated with an episode of caldera collapse, caused the rapid drainage of their lava lakes (Neal et al. 2019; Shreve et al. 2019).

In this study we investigate the mechanism behind the 2018 Ambrym eruption. We present petrological observations of glasses, crystals and melt inclusions of both the initial intra-caldera fire-fountain eruption and subsequent submarine eruption. We then compare these findings to geophysical and surficial observation to derive a detailed understanding of the cause and timing of the eruption as well as the architecture of Ambrym's plumbing system.

THE 2018 ERUPTION OF AMBRYM VOLCANO

A detailed account of the temporal evolution of the eruption in terms of deformation, seismic, thermal and SO_2 gas emissions from ground and satellite observations is given in Shreve et al., (2019). Here we summarise the main events focussing on the deposits and ground observations. We divide the eruption in two parts, the intra-caldera and the submarine eruption.

Intra-caldera eruption

On 14 December 2018 (all date and time in UTC), the volcano-seismic crisis began with a few events detected inside the caldera. Lava reached the surface around 23h20 UTC from two fissures according to high time-resolution thermal observations from Advanced Himawari Imager (AHI) aboard HIMAWARI 8 geostationary satellite (Shreve et al. 2019). Two fissures opened, one trending N110° at 590 m a.s.l. and cutting through the Lewolembwi tuff ring (re-activation of a pre-existing fracture) and the other trending N-S at 730 m a.s.l. and located near the eruption site of the 2015 lava flows. The first fissure produced mainly scoria deposits covering a 1 km radius (with minor pahoehoe lava flows close to the eruption site) while the second fissure produced a blocky, 10^6 m^3 (Shreve et al. 2019) lava flow (Fig. 1, panel 6, 7 and 8). Both fissures likely resulted in fire fountain style of eruption (visually confirmed only at the second fissure). As lava extrusion proceeded on the SE flank of the volcano during the 15 of December, lava lake activity at the summit ceased according to satellite thermal observations (Shreve et al. 2019). Directly prior to the eruption, five lava lakes were being observed by the authors in the summit region, two at Benbow and three at Marum (with lake level at Marum's main lava lake noticeably increasing in the weeks prior to the eruption; Fig. S1) (Fig. 1, panel 1 and 2). The crater walls around all five lava lakes had partially collapsed inward by 16 December, one lava lake at Marum crater had been replaced by a water lake at that time. A previously vigorously degassing vent located just south of Marum (called Maben Mbwelesu or

Niri Taten, source of the 1988–1989 basaltic lava flow) also ceased degassing (Fig. 1, panel 3). According to HIMAWARI observations, syn-eruptive SO_2 degassing mainly took place on 15 and 16 December, ceasing early in the morning of 16 December (UT) (Shreve et al. 2019). On 15 December at 17:45 and 19:45 and on 16 December at 1:00 and 5:00 ash clouds were observed from the Vanuatu Meteorology and Geohazards Department's webcam. On 16 December at 3:30, lahars were observed on the flank of both Benbow and Marum (Fig. 1, panel 5). Yet no rainfall had been reported since the onset of the eruption, suggesting that the water originated from within the edifices, possibly as a result of compaction during the period of subsidence highlighted by InSAR observations (see next section). By the end of December 16, surficial activity inside the caldera had ceased. Videos from a helicopter overflight in the caldera on 16 December are provided in the supplementary.

Dike propagation and submarine eruption

At 20h21 on December 15 the seismic activity increased sharply marking the beginning of magma propagation into the SE rift zone (Shreve et al., 2019). By 17 December at 12:00, inversion of InSAR data revealed ~3 m of opening along a >30 km long dike, of 419 to 532x10^6 m^3 total volume, dipping ~70° to the south, and extending from within the caldera to beyond the eastern coast (Shreve et al., 2019). Around 16:00 on December 17 magma migration stopped, likely marking the onset of a shallow submarine eruption just off the SE coast of Ambrym, near the villages of Pamal and Ulei, confirmed in the following days as basaltic pumice drifted to shore. This large magma migration episode in the subsurface was accompanied by inflation in the SE part of the island (Fig 1, panel 4) but also by subsidence (>2 m) of the caldera floor (Shreve et al., 2019).

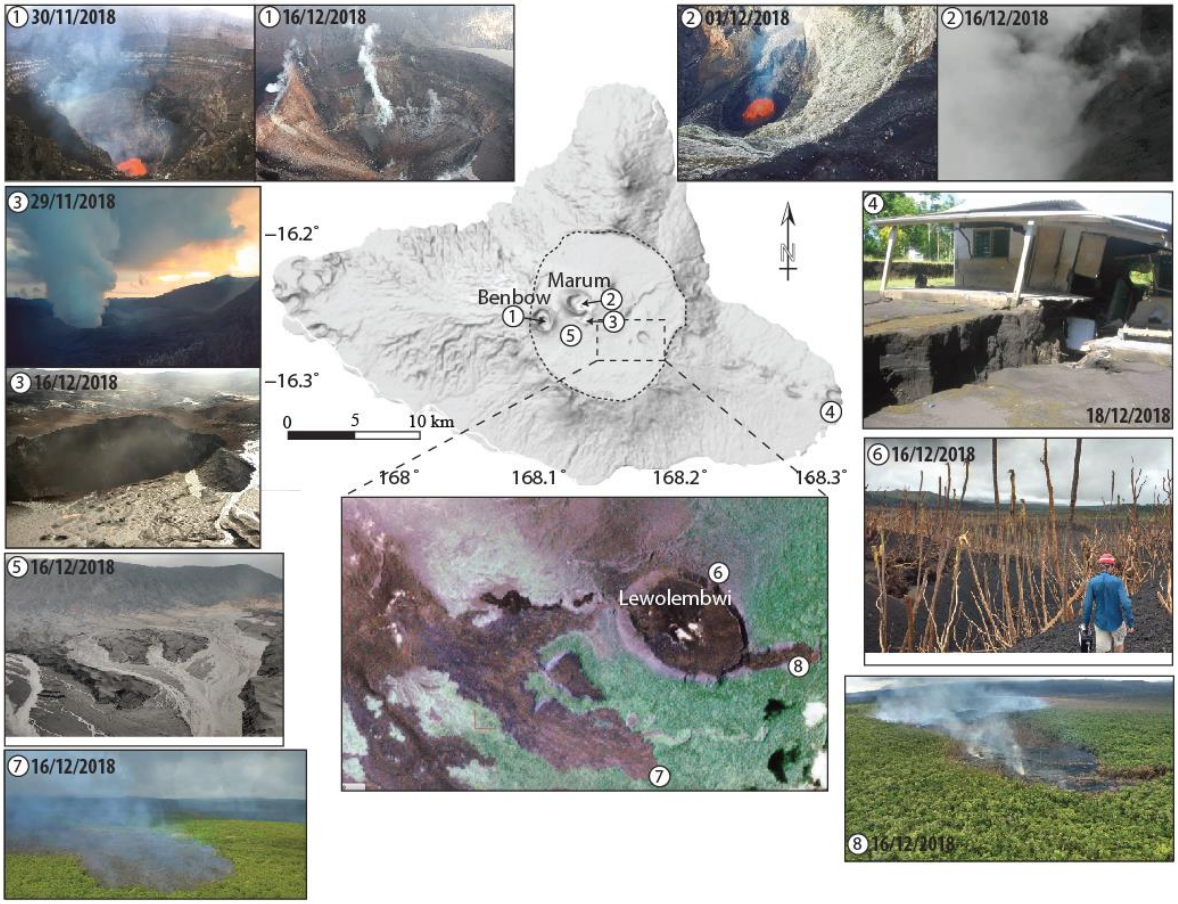

123

124 ***Fig. 1*** *Central panel: shaded hillside view of Ambrym Island (source CNES/Airbus), dotted*
125 *contour outlines the ~12 km diameter caldera. Lower panel: True-colour Planet image taken*
126 *on 31-02-2019 showing the extent of lava flow and scoria deposits (emplaced on 14-16*
127 *December 2018). Numbers on the central and lower panels show the location of the*
128 *photographs with corresponding numbers. Panel 1 shows one of two lava lakes at Benbow*
129 *crater before and after/during the eruption. Panel 2 shows one of three lava lakes at Marum*
130 *crater before and after/during the eruption. Crater walls around all five original lava lakes*
131 *partially collapsed, one lava lake was replaced by a water lake by December 16. Panel 3 shows*
132 *the Maben Mbwelesu or Niri Taten vent before and after/during the eruption. Panel 4 shows*
133 *the surface deformation and resulting fracturing affecting the coastal village of Pamal, located*
134 *close to the site of inferred submarine eruption starting on 17December. Panel 5, view of*
135 *Marum with lahar coming down the flanks of the edifice from all direction whilst no rainfall*
136 *had occurred, suggesting that groundwater, expelled due to compaction was generating the*
137 *mud flows. Panel 6, view from the flank of Lewolembwi crater with palm trees blasted and*
138 *partially buried by scoria. Panel 7, view of the lava flow with active front marked by burning*
139 *vegetation. Panel 8, view of the fissure running through the Lewolembwi crater*
140

METHODOLOGY

Samples

Tephra samples from the intra-caldera eruption were collected on 16 December 2018, North of the Lewolembwi crater (at 16°16'3.65"S; 168°10'13.61"E, sample name AMB2018_FF_S1 and at 16°15'42.42"S; 168°10'17.41"E, sample name AMB2018_FF_S2). Tephra from both samples were lapilli-size but sample AMB2018_FF_S2, being located further from the fissure was composed of smaller (typically < 1cm diameter) lapilli. An ash sample was collected south of the Marum and Benbow craters (at 16°16'4.29"S; 168° 7'3.24"E, sample name AMB2018_FF_S3). Tephra samples from the submarine eruption were collected on 18 December 2018 (sample name AMB2018_SUB_S1) and 04 February 2019 (sample name AMB2018_SUB_PAMAL_1) from the beach near the coastal village of Pamal. In both cases the pumices were floating and deposited onshore. The exact timing of the deposition of each wave of scoria is unknown. Both samples consist of lapilli size (typically < 1cm diameter), highly vesicular fragments. Details on sample processing are provided in the supplementary.

Analyses of major, trace and volatile elements

Major element compositions of bulk tephra were analysed on a HORIBA-Jobin-Yvon ULTIMA C ICP-AES at Laboratoire Magmas et Volcans in Clermont-Ferrand using the procedure described in Moussallam et al. (2019). Trace element compositions of melt inclusions and glasses were analysed using a laser ablation system associated with an inductively coupled plasma mass spectrometer of the Laboratoire Magmas et Volcans, Clermont-Ferrand (193 nm Excimer Resonetics M-50E laser with an Agilent 7500 ICP–MS). Volatile (H_2O, CO_2, Cl, F, S) content in melt inclusions, embayments, and matrix glasses were determined using a Cameca IMS 1280 ion microprobe at CRPG-CNRS-Nancy. Analytical conditions were similar to other volatile studies (e.g., Hauri et al. 2002; Bouvier et al. 2008;

Shimizu et al. 2009; Rose-Koga et al. 2014, 2020.; Moussallam et al. 2015b, 2019). Details of all three methods are provided in the supplementary.

Volatile and olivine diffusion modelling

Concentration profiles recorded in the embayments were fitted by a diffusion model similar to the one of Ferguson et al. (2016), building on the model presented in Moussallam et al. (2019). Chemical gradients (Fe–Mg, Mn and Ca) in olivine crystals were modelled in one dimension using the DIPRA software (Girona and Costa 2013). Details of both methods are provided in the supplementary.

Assessment of post-entrapment crystallisation.

The amount of post-entrapment crystallisation (PEC) for olivine-hosted inclusions was estimated using the Petrolog3 software (Danyushevsky and Plechov 2011). Calculations were performed using the olivine-melt model of Danyushevsky, (2001), the density model of Lange and Carmichael, (1990), the model for melt oxidation of Kress and Carmichael, (1988) and the model of Toplis, (2005) for the compositional dependence of the olivine-liquid Fe-Mg exchange coefficient (Kd). Calculations were performed assuming a system buffered at the nickel nickel-oxide (NNO) equilibrium. Note that calculations in Petrolog3 are performed under anhydrous conditions at 1 atm. As the inclusions showed no sign of iron loss (Fig. 3D), measured FeOt concentration were taken as final concentration. The resulting PEC estimates range from -10 to 5% with an average of -3% and standard deviation of ±3%. Performing the same calculations at the quartz-fayalite-magnetite (QFM) buffer yield similar results with a range from -11 to 3%, an average of -4% and standard deviation of ±3%. Given that most (77%) olivine-hosted inclusions are modelled to have undergone no or negative amounts of PEC we consider that is can safely be assumed that most inclusion have retained their

entrapment composition and not been affected by any significant amounts of PEC. In addition, the fact that olivine-hosted melt inclusions, pyroxene-hosted melt inclusions and matrix glasses all record the same range in compositions argues against any significant post-entrapment crystallisation effect on the melt inclusion compositions.

RESULTS

Mineralogy and texture

The bulk of the eruptive products is composed of glassy, crystal-poor, mafic scoriae containing numerous round vesicles (Fig. 2A). There is no significant difference between the subaerial and submarine scoriae. Microlites (< 200 μm) are predominantly plagioclase, with small amounts of olivine, clinopyroxene, and magnetite. Larger crystals are rare, and include olivine and plagioclase phenocrysts, sometimes associated with magnetite. Glomerocrysts composed of olivine, clinopyroxene, plagioclase, and magnetite (Fig. 2B) are relatively frequent, and often coated by a darker glass, with a more silicic composition than the dominant mafic glass. Evidence of mingling at the microscopic scale between a mafic glass and a silicic glass has been observed in all eruptive products (Fig. 2C), although the silicic component is always subordinate, and no macroscopic sample with a dominant silicic composition has been found. Apart from the glomerocrysts, the silicic glass often contains plagioclase microlites. There is also evidence of mingling between the phenocryst-poor mafic melt, and a third component with a similar mafic composition but a higher crystallinity (Fig. 2D), indicating that at least three different magmas were erupted at the same time.

Olivine phenocrysts show a bimodal distribution (Fig. 3A; Table S2; S3 and S4), with a main population around Fo_{74} in equilibrium with the mafic magma (Fe/Mg olivine Kd of 0.30 ± 0.04), and a second population around Fo_{66} in equilibrium with the silicic magma (Fe/Mg

olivine Kd of 0.30 ± 0.04). Most low Mg# and high Mg# olivines (37 / 45) are usually homogeneous. However, when included in the mafic magma, low-Mg# olivines show rounded shapes indicative of dissolution (Fig. 2E), and a small rim with a higher Mg# (four crystals, hereafter called type 1 reverse zoning). Another four olivine crystals (two from each population) show a more pronounced, large scale reverse zoning (type 2 reverse zoning, see timescales section below). Olivine phenocrysts also often contain glassy melt inclusions that preserve the composition of their parent magma (Fig. 2G). A few high-Mg# olivine crystals contain large numbers of inclusions and embayments (Fig. 2H), a texture possibly acquired through initial skeletal growth or as a result of dissolution. Clinopyroxene crystals mostly belong to the glomerocrysts originating from the silicic magma and have an average Mg# of 72 (Fig. 3B). Some of those clinopyroxene crystals show evidence of multiple growth stages, dissolution, and oscillatory zoning (Fig. 2F), indicating a protracted history for the cooling and crystallization of the silicic magma. Composition of plagioclase phenocrysts vary from An_{85} to An_{48}.

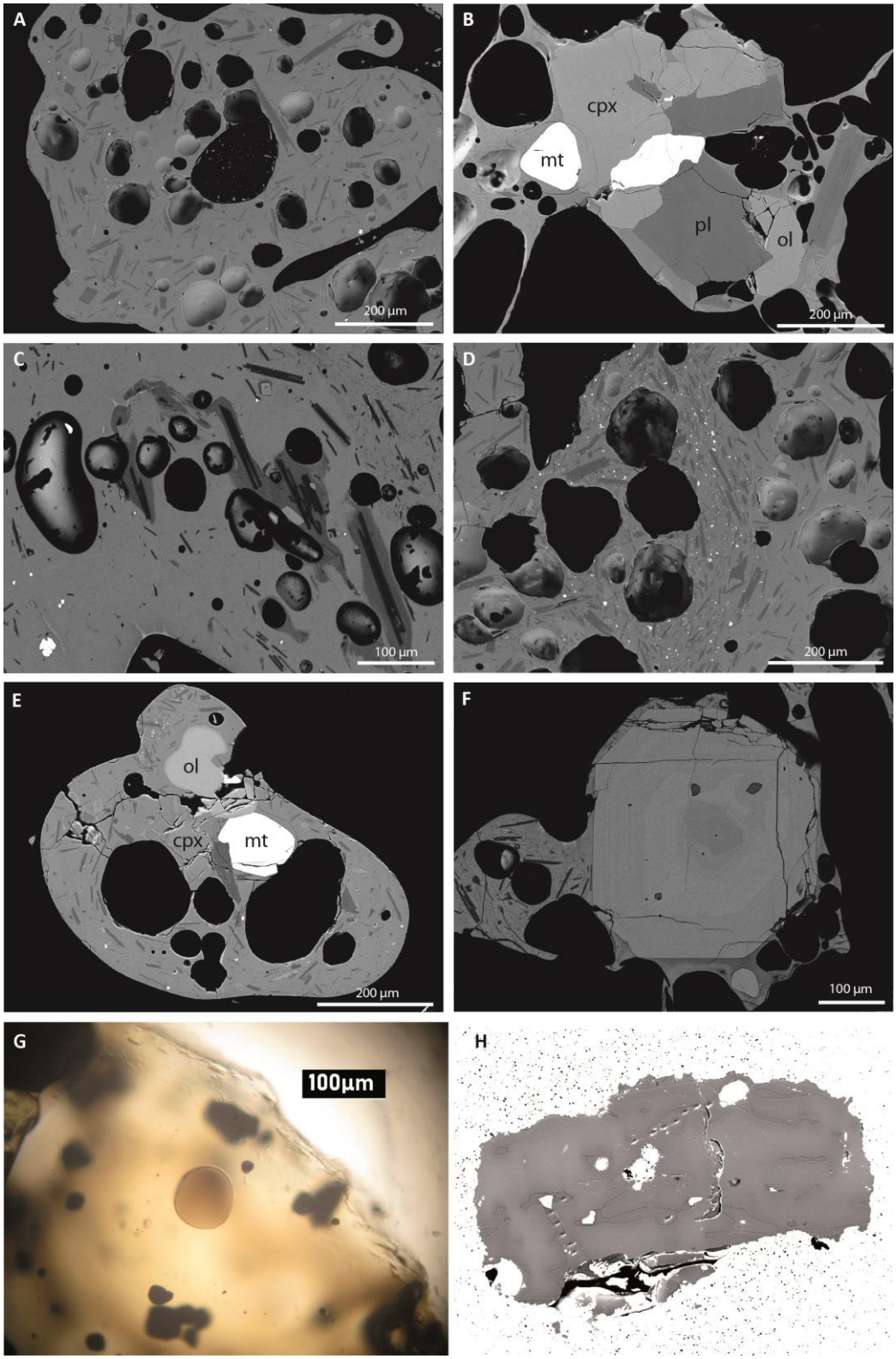

Fig. 2 A-F. *BSE microphotographs of typical textures for subaerial and submarine eruptive products:* ***A.*** *Typical texture of the dominant, crystal-poor mafic magma, with microlites of plagioclase and minor olivine, clinopyroxene and magnetite.* ***B****. Plagioclase-clinopyroxene-olivine-magnetite glomerocryst surrounded by a small layer of microlite-free silicic melt (darker grey) within a more microlite-rich mafic melt.* ***C****. Mingling between a crystal-poor mafic melt (lighter grey, dominant) and a silicic melt (darker grey with darker plagioclase*

microlites, less abundant). The upper right side of the picture shows a mafic melt with higher crystallinity. ***D****. Mingling between a crystal-poor and a crystal-rich mafic melts. Both melts contain the same microlite assemblage of plagioclase, olivine, clinopyroxene and magnetite, with less magnetite in the crystal-poor melt.* ***E****. Another glomerocryst from the silicic melt, now partially dissolved in the mafic melt, with a thin magnesian overgrowth rim around the olivine crystal.* ***F.*** *Clinopyroxene megacryst, surrounded by a small amount of silicic glass (dark grey, bottom of picture), in turn surrounded by mafic, microlite-rich glass (left). Evidence of multiple growth stages, dissolution, and oscillatory zoning indicates a protracted history for the silicic magma. Dark glassy melt inclusions in the megacryst core have a trachydacitic composition.* ***G.*** *Transmitted light optical microphotograph of an olivine crystal with a glassy melt inclusion.* ***H.*** *BSE microphotograph of an olivine crystal with numerous glassy melt inclusions and embayments (black spots are from SIMS analyses)*

Major elements

The major element composition of melt inclusions, embayments and matrix glasses is given in Tables S1 and reported in Fig. 3 together with bulk rock, matrix glass and melt inclusion analyses from the literature. The composition of melt inclusions and matrix glasses from the 2018 Ambrym eruption is bimodal with modes centred around ~53 and ~60 wt.% SiO_2 and compositions ranging from 50 to 63 wt.% SiO_2. Melt inclusions from both the intra-caldera and submarine eruptions capture the full range of compositions. Matrix glasses from the onset of submarine eruption however (sample collected on 18 December 2018, labelled initial phase on subsequent figures) shows very restricted basaltic trachy-andesite composition with no trachy-andesite to trachy-dacite component as opposed to matrix glasses from subsequent submarine eruptive activity (sample collected on 04 February 2019) which show both components and very limited intermediate compositions (i.e. limited chemical mixing). Most pyroxene-hosted melt inclusions (yet not all) are of the more evolved composition while olivine-hosted melt inclusions are of both components with very limited intermediate compositions. This is in agreement with the presence of two populations of olivine phenocrysts and only one population of clinopyroxene phenocrysts (Fig. 3 A, B). Bulk compositions of the intra-caldera and submarine eruptions are both basaltic trachy-andesite. Melt inclusions have Mg# ranging from 24 to 60 (assuming all iron is FeO). Host olivine crystals have compositions

ranging from Fo_{65} to Fo_{76} with no systematic difference between melt inclusions and olivine from intra-caldera and submarine eruptions. The range of observed composition from the 2018 eruption is covered by bulk rock analyses of older deposits. Evolved compositions are rare at Ambrym, the one reported here are similar to the high-potassium (HK) andesite to dacite series described by Picard et al. (1994) previously found only around the Lewolembwi crater. The more primitive compositions reported here on the other hand are typical of the recent historic trachy-basaltic to basaltic trachy-andesite activity, very close in composition to that reported for bulk, matrix glass and melt inclusions in recent deposits of lava expelled from Marum and Benbow craters (Firth et al. 2016; Allard et al. 2016a; Sheehan and Barclay 2016) (Fig. 3). The observed range in melt inclusion compositions can be mostly explained in term of mixing between two end members, a more trachy-basaltic (at ~51 wt.% SiO_2) and a more trachy-dacitic (at ~63 wt.% SiO_2) component (estimated end member compositions given in Table S1).

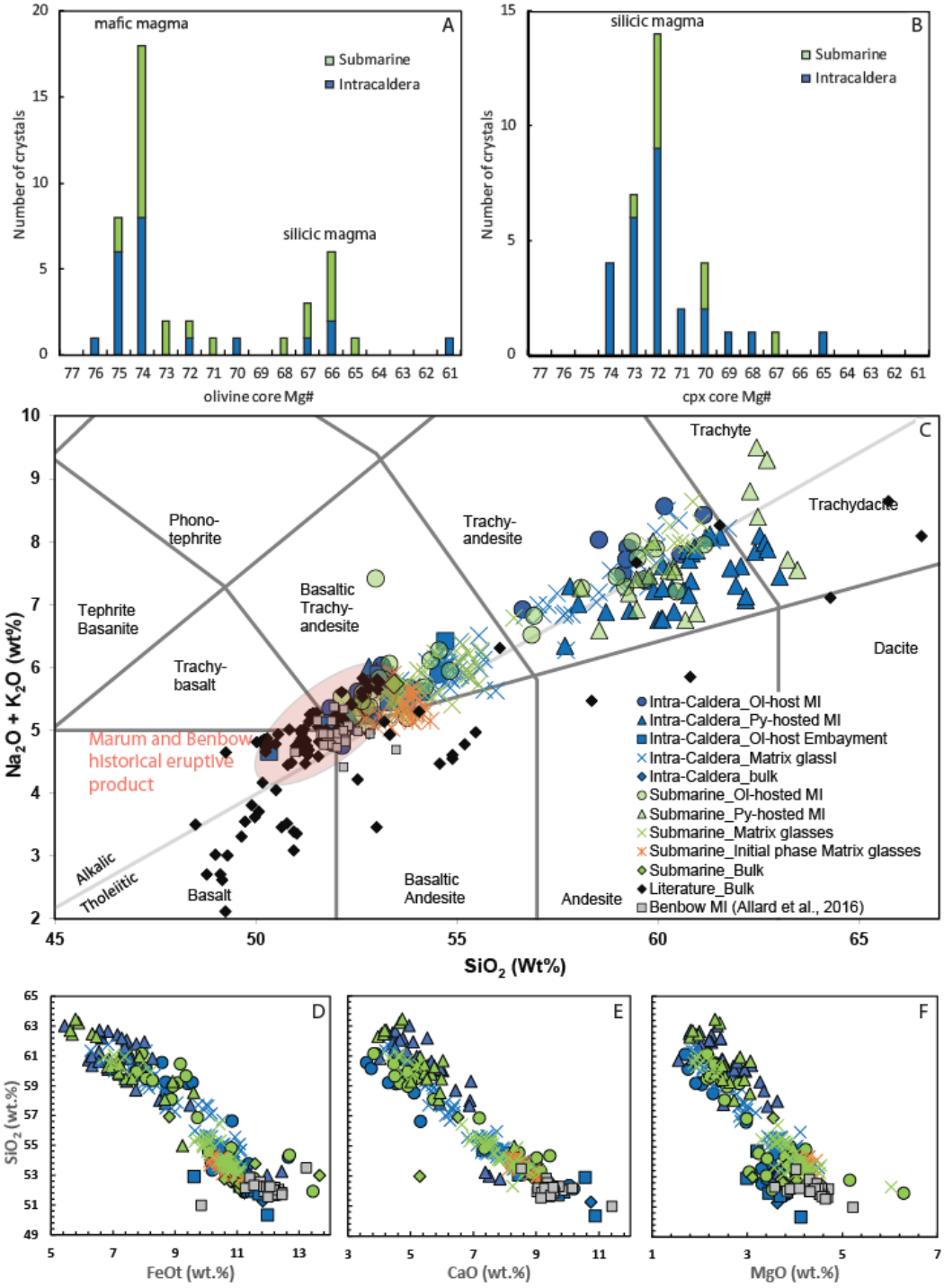

***Fig. 3 A**. Frequency diagram of the Mg# of olivine cores from the intra-caldera and submarine eruptions. **B**. Frequency diagram of the Mg# of pyroxene cores from the intra-caldera and submarine eruptions. **C**. Total alkalis vs silica. Melt inclusions, matrix glasses, and bulk rock compositions (all normalized to 100% on a volatile-free basis) for the 2018 intra-caldera (blue symbols) and submarine (green and orange symbols) eruptions. Bulk rock literature data are from locations covering the entire island* (Gorton 1977; Picard et al. 1994; Firth et al. 2016; Allard et al. 2016a; Sheehan and Barclay 2016). *Faded pink ellipse shows the typical composition of bulk lava, matrix glasses and melt inclusions from 1913 to 2014 eruptive products from Marum and Benbow craters* (Firth et al. 2016; Allard et al. 2016a; Sheehan and Barclay 2016). ***D**, **E** and **F**. SiO_2 vs FeO_{tot}, CaO and MgO diagrams*

Trace elements

Trace and rare earth elements concentrations in melt inclusions and matrix glasses are reported in Table S5 and show no systematic differences between the intra caldera and submarine eruptions albeit limited data. Highly incompatible elements define positive linear correlation offset from the origin (Fig. 4A-C) suggesting mixing between two components or evolution through partial melting (fractional crystallization is expected to result in linear correlation passing through the origin, e.g., Schiano et al. 2010). Plots of incompatible trace element ratios versus abundance (Fig. 4D and E) show a positive correlation also consistent with either mixing or partial melting (as fractional crystallization would result in no variations of the ratio with concentration, e.g., Schiano et al. 2010).

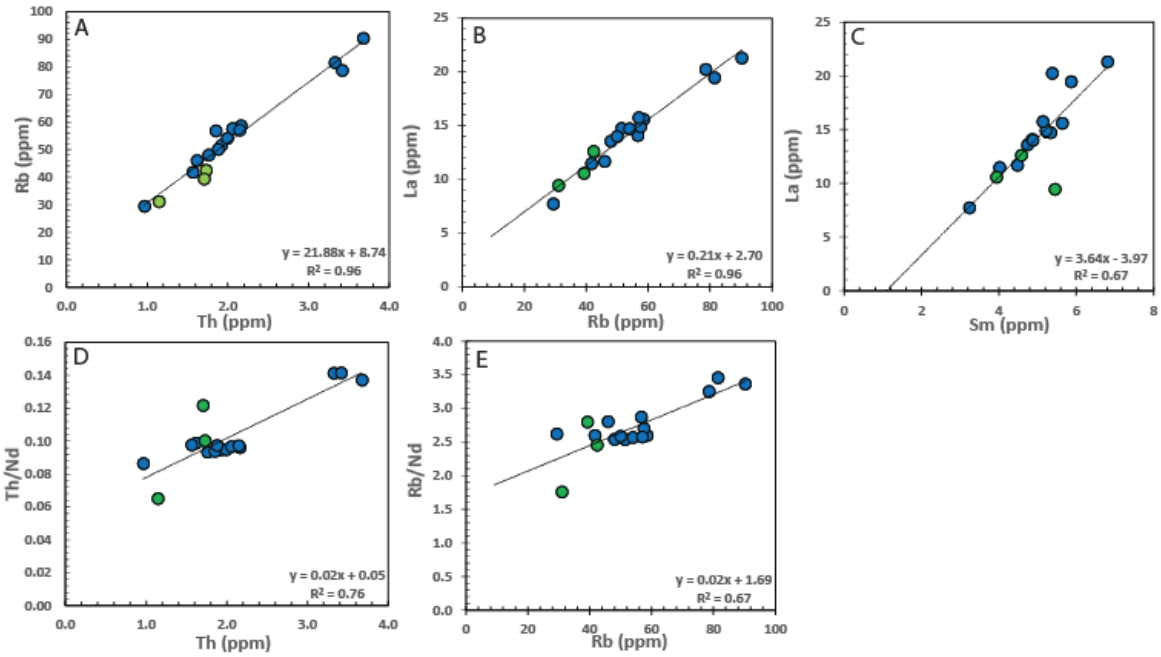

Fig. 4 *Trace-element variation diagrams from melt inclusions and matrix glasses from the intra-caldera (blue) and submarine (green) eruption.* ***A****. Plot of Rb vs Th.* ***B.*** *Plot of La vs Rb.* ***C****. Plot of La vs Sm.* ***D****. Plot of Th/Nd vs Th.* ***C****. Plot of Rb/Nd vs Rb. Linear regression lines through all data are presented on each plot*

Volatiles

Volatile contents from melt inclusions, embayments and matrix glasses from both the intra-caldera and submarine eruptions are given in Table S6. In melt inclusions and matrix glasses, chlorine ranges from below detection to 1200 ppm, fluorine from 200 to 1000 ppm, water from below detection to 2.1 wt.%, CO_2 from below detection to 1800 ppm and sulfur from below detection to 1700 ppm. H_2O and CO_2 values in melt inclusions are regarded as minimum values from the time of entrapment given that H^+ diffusion out of the melt inclusion (e.g., Chen et al. 2011) and CO_2 diffusion in shrinkage bubbles (e.g., Anderson and Brown 1993) cannot be discarded.

CO_2 vs H_2O abundance in melt inclusion does not follow a single degassing trend but might instead reflect the combination of several distinct degassing paths. Sulfur abundance is partly controlled by degassing as evidenced by the systematic difference between melt inclusions and matrix glasses. The presence of sulfides in some melt inclusions (Fig. 5) indicates that the melt must have been at saturation with a liquid sulfide phase prior to ascent and degassing. The large size of the sulfides (~20 µm, Fig. 5 and MI photographs in appendix) precludes their formation from secondary processes. This is further indicated by the observed negative correlation between the maximum sulfur content of melt inclusions and their FeO content following the expected trend of sulfur content at sulfide saturation (Fig. 5). Both chlorine and fluorine contents are correlated with melt composition, the basaltic melts end member having around 450 ppm Cl and 550 ppm F and the dacitic melt end member having around 1100 ppm Cl and 800 ppm F. The original water content of the more mafic and more silicic melts mostly overlaps, although the mafic component has melt inclusions with low (<0.75 wt.%) water content that are largely absent from the more silicic component indicating more extensive shallow crystallisation. Mafic melt inclusions from the submarine eruption tend to record

higher water and CO_2 content than mafic melt inclusions from the intra-caldera eruption. There are no correlations between the melt inclusion CO_2 content and their major element composition.

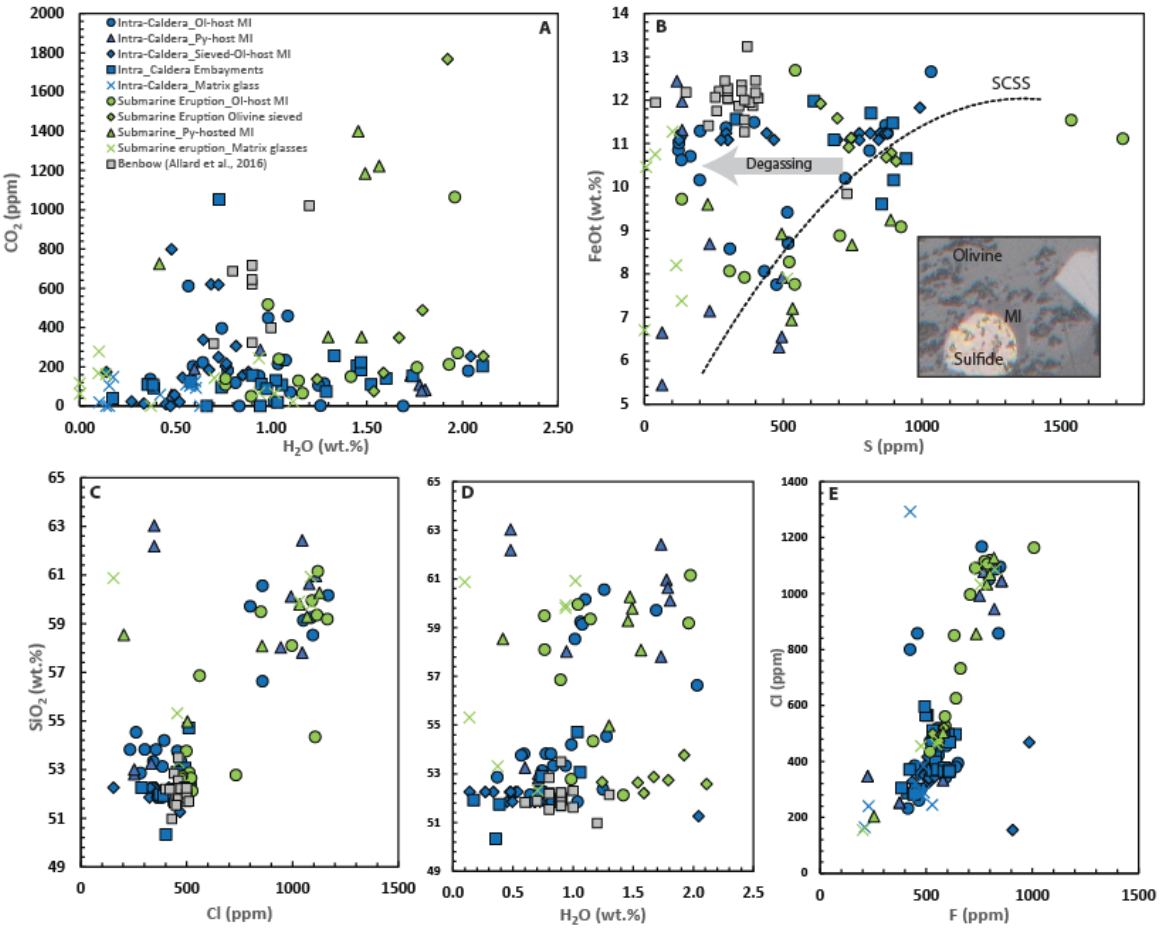

Fig. 5 *Volatile elements abundance in melt inclusions, embayments and matrix glasses from Ambrym. Inset: reflected-light microphotograph showing a ~20µm sulfide in an olivine-hosted melt inclusion (olivine AMB A12). Dotted curve on panel B show calculations of the sulfur content at sulfide saturation (SCSS) calculated at 1200°C, 100 MPa using the model of Smythe et al. (2017)*

Geothermobarometry and volatile saturation pressure

Melt inclusions entrapment pressures were calculated using the model of Iacono-Marziano et al., (2012) for H_2O-CO_2 saturation pressure. They yield entrapment pressures between 5 and 280 MPa (Fig. 6). Given the above-reported error on the volatile content determination and the error on the model, the results can conservatively be taken to be precise at ± 20%. Yet, as

352 discussed previously, H_2O and CO_2 values are to be considered as minimum values due to
353 possible diffusion of both species. The entrapment pressures are therefore also to be taken as
354 minimum pressure estimates. Another reason to assume these pressure estimates are minimum
355 is that the model of Iacono-Marziano et al., (2012) that we use here has been shown, at least
356 for alkali basalt compositions to overestimate the amount of water that can be in dissolved in
357 the melt (see Fig. 13 in Shishkina et al. 2014).
358
359 Shown in Fig.6 is the absence of systematic difference between the entrapment pressures of
360 the more basaltic and the more dacitic melt inclusions. Both magmas appear to have
361 crystallized over similar pressure ranges. Similarly, we see no strong systematic differences
362 between the entrapment pressure of melt inclusions from crystals erupted during the intra-
363 caldera and those erupted during the submarine eruption, although we note that the five most
364 deeply entrapped (180 to 280 MPa) inclusions are all from crystals erupted in the submarine
365 eruption suggesting contribution from a deeper magma that was not present in the intra-caldera
366 eruption. Similarly, all the most shallowly entrapped (< 24 MPa) melt inclusions are from
367 crystals erupted during the intra-caldera eruption suggesting that the shallowest (top 750 m)
368 portion of the magmatic system contributed only to the intra-caldera eruption and might have
369 been emptied prior to the submarine eruption.
370 The volatile content of matrix glasses erupted during the submarine eruption should
371 theoretically reflect the hydrostatic pressure under which they were erupted. Volatile contents
372 indicate pressures of last equilibration in the range of 2.5 to 50 MPa. We attribute this large
373 range to the rapid ascent (see ascent rates section) that would have impeded equilibrium
374 degassing (Pichavant et al. 2013) and to the potentially explosive nature of the submarine
375 eruption preventing re-equilibration at extrusion pressure. Taking the lowest recorded

376 equilibrium pressure as the maximum emplacement depth suggests that the submarine eruption
377 took place less than 250m underwater.
378

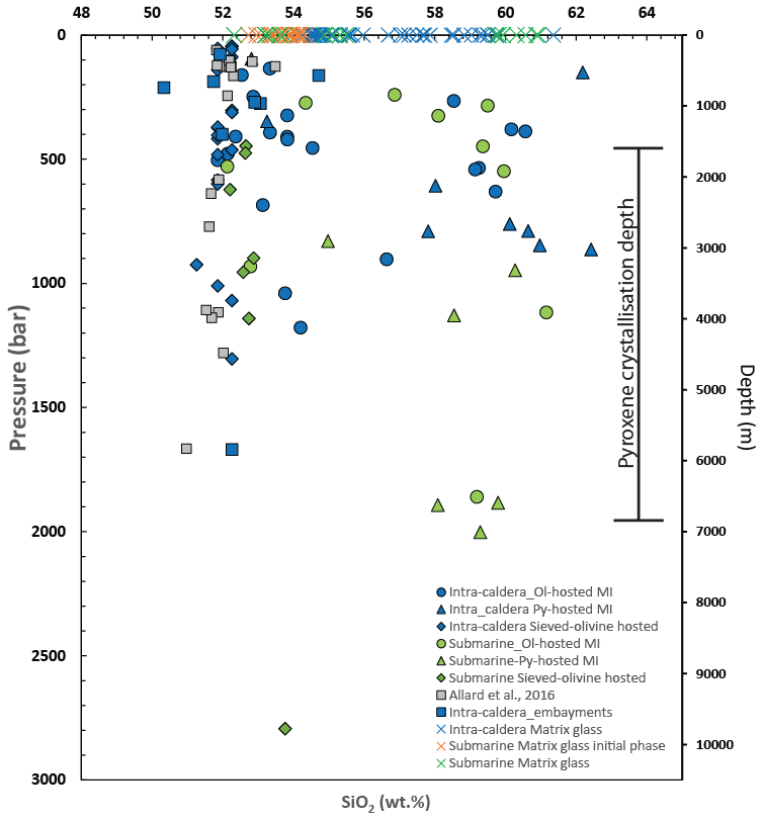

379

380 ***Fig. 6*** *Melt inclusions entrapment pressure calculated from H_2O-CO_2 saturation pressure*
381 *using the model of Iacono-Marziano et al., (2012) for all data shown including the data from*
382 *Allard et al., 2016, compared to melt SiO_2 content. Note that all matrix glasses are arbitrarily*
383 *plotted at 1 bar*
384

385 Since all glasses are saturated with olivine, pre-eruptive temperatures were calculated using the
386 olivine-melt thermometers of Ford et al. (1983) and Beattie et al. (1993). Both thermometers
387 give near-identical results for the mafic glasses (Ford: 1125 °C; Beattie: 1112 °C; average of
388 1120 °C). The silicic melt was slightly colder, with estimated temperatures between 1074
389 (Beattie) and 1112 °C (Ford), for an average temperature of 1100 °C. Taking into account a
390 1.2 wt% water content in the magma (average of all analysed melt inclusions) results in lower

391 estimated pre-eruptive temperatures of 1078 °C for the mafic magma and 1054 °C for the silicic
392 magma, using the model of Médard and Grove (2008).
393 Previous work on clinopyroxene-based thermobarometry for the 2005-2007 eruptive products
394 of the then-active lava lakes were published by Sheehan and Barclay (2016). Using three
395 different thermometer/barometer combinations (Putirka et al. 2003; eq. (32a) and (32d) of
396 Putirka et al. 2008; eq. (30) and (33) of Putirka et al. 2008), they report a tight range of average
397 storage pressures for Mg#74-76 clinopyroxenes between 390 and 485 MPa. Work on a larger
398 range of eruptive products (from 1913 to 2014, clinopyroxenes Mg#61-74) by Firth et al.
399 (2016) using eq. (30) and (33) of Putirka produces a similar pressure range of 433 ± 86 MPa
400 (excluding one of their datapoint at 1000 MPa). Using the same eq. (30) and (33) of Putirka et
401 al. (2008) on 14 Mg#70-74 clinopyroxenes from the 2018 eruptive products associated with
402 melt inclusions returns average crystallisation pressures of 145 ± 59 MPa at temperatures of
403 1042 ± 25 °C, in excellent agreement with the pre-eruptive temperature for the silicic magma
404 estimated from olivine-melt thermometry. There is no overlap between our dataset and
405 previous datasets (Sheehan and Barclay 2016; Firth et al. 2016), suggesting that two different
406 storage levels were sampled by the 2018 eruption and previous eruptions. Since most
407 clinopyroxene crystals (if not all) come from the silicic magma, we use an average melt
408 composition of the silicic melt inclusions, and average water content of 1.2 wt% to apply the
409 same combination of thermometer and barometer to a larger dataset of 81 clinopyroxene
410 phenocryst analyses. The resulting pre-eruptive pressure is 121 ± 75 MPa at a temperature of
411 1034 ± 8 °C, identical to the values obtained with the more restricted dataset. Although using
412 the same barometer, no value came within error of the pressures determined by Firth et al.
413 (2016) and Sheehan and Barclay (2016), confirming that the 2018 eruption sampled a shallower
414 storage system than previous eruptions. Assuming a crustal density of 2900 $kg.m^{-3}$, those
415 crystallization pressure translates into crystallization depths of 4.3 ± 2.6 km (or 5.1 ± 2.1 km

for the restricted dataset of inclusion-bearing clinopyroxene phenocrysts), in excellent agreement with the deeper part of the storage system imaged through saturation pressure of melt inclusions (see also Allard et al. 2016a).

Residence time

The eight olivine crystals that showed significant (greater than 2 %) differences in their forsterite content were investigated through detailed (1 to 10 µm step) compositional EMP profiles. All 8 crystals record reverse zoning with core compositions around Fo_{65} to Fo_{70} and rim compositions around Fo_{70} to Fo_{76}. These reversely zoned crystals are rare because the more silicic magma is volumetrically much smaller than the primitive one and contains much fewer olivine (Fig. 3). As a result, the vast majority of olivine crystals in the mixed deposit are from the mafic component and are in equilibrium with the carrier melt, which is dominantly of mafic composition, hence showing no significant zoning. The chances of finding olivine crystals from the silicic component that have been in contact with the mafic component and started re-equilibrating diffusively are small and only 8 such reversely zoned olivine crystals were found. Two very different diffusion profiles are recorded by these crystals; type 1 profiles (4 crystals) show very sharp compositional variations occurring over a narrow 5 to 20 µm distance to the crystal edge, while the other 4 (type 2 profiles) show very smooth core to rim compositional variations occurring over distances greater than 60 µm from the crystal edge. Diffusion profiles for these 4 crystals could not be modelled accurately as a clear "plateau" in terms of composition was not constrained. Their profiles however are consistent with strict minimum diffusion timescales on the order of years. The four crystals that displayed sharp compositional profiles were modelled using the DIPRA software (Girona and Costa 2013) for diffusion timescale using the variations in Fe-Mg, Mn, Ni and Ca content. Results together with the full list of parameters used for the modelling are given in supplementary Table S7. Modelled Fe-

441 Mg, Mn and Ni diffusion profiles match the natural data extremely well and yield similar time
442 estimates (Fig. 7) confirming that these natural profiles are the result of diffusion and not
443 growth processes. Modelled Ca diffusion profiles tend to have much higher discrepancy, carry
444 large uncertainties, and do not always yield diffusion timescales consistent with those obtained
445 from the Fe-Mg, Mn and Ni diffusion profiles. Any modelled diffusion profile yielding ≥15%
446 discrepancy with the data was discarded.
447
448 Of the four olivine crystals for which diffusion timescale was investigated, one is from the
449 intra-caldera eruption while the other three are from the submarine eruption. The crystal from
450 the intra-caldera eruption record compositional profiles consistent with a diffusion timescale
451 of less than a day. Olivine crystals from the submarine eruption record compositional profiles
452 consistent with diffusion timescales of about two days indicating that mixing of these olivine
453 crystals (originating from the silicic magma) into the more primitive magma took place one to
454 a few days prior to eruption (Fig. 8).
455
456 The presence of four olivine phenocrysts with diffusion profiles indicative of long-term
457 diffusion, as well as frequent oscillatory zoning within the clinopyroxene phenocrysts indicate
458 the possibility of periodic interaction between the silicic and mafic magmatic systems, with at
459 least one interaction occurring more than a year prior to the 2018 eruption.
460

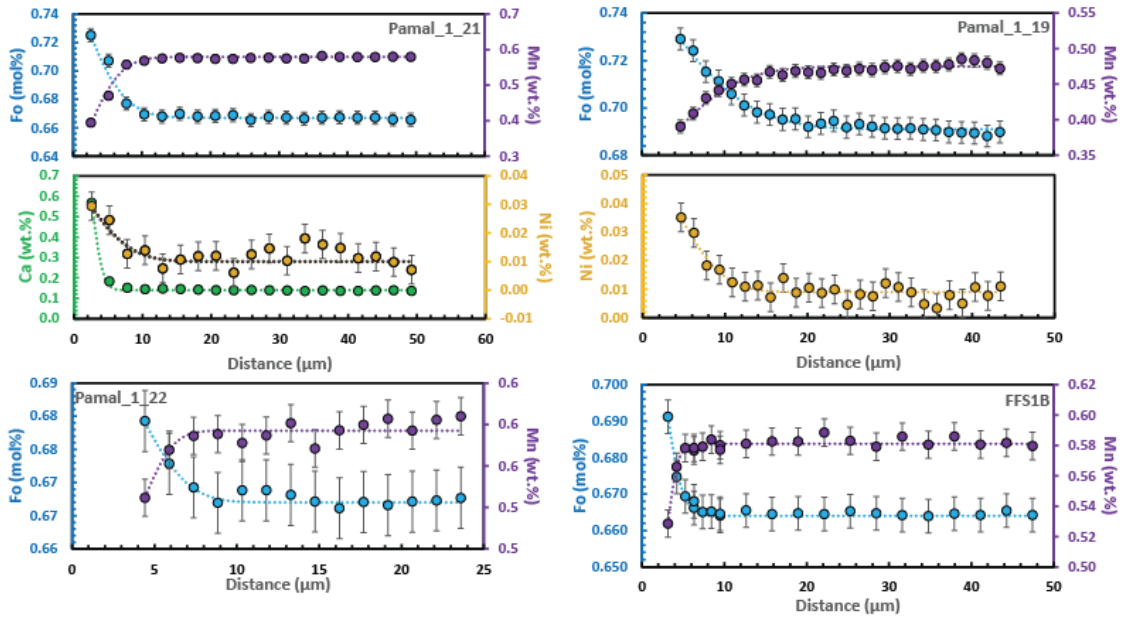

461

462 ***Fig. 7*** *Results of diffusion modelling (dotted lines) compared to Fo, Mn, Ni and Ca*
463 *concentrations profiles (measured by EMPA, error bars are 2σ) in four olivine crystals from*
464 *the intra-caldera and submarine eruptions. Modelling was performed using the DIPRA*
465 *software* (Girona and Costa 2013)
466

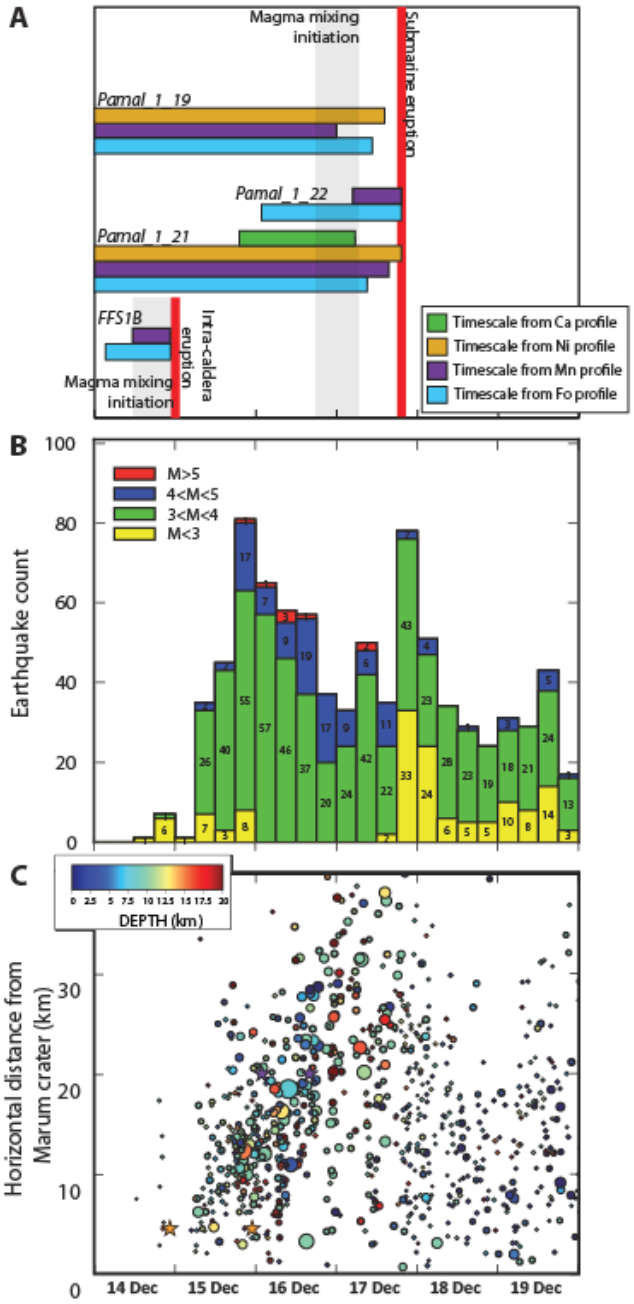

***Fig. 8 A**. Summary of diffusion timescales obtained from modelling Fo, Mn, Ni and Ca diffusion profile. Each coloured bar shows the range of possible diffusion timescale taking into account unknown crystal orientation (modelling along the a and c axes) and the error on each diffusion model (derived from 2σ error on EMPA and a 25°C error on the estimated temperature). Note that calculated diffusion timescale, obtained in unit of time, are presented here in term of date assuming that diffusion stopped at the onset of eruption. The time window where all diffusion timescale overlap is taken to represent the time at which diffusion started which we interpret as the initiation of magma mixing (time at which olivine crystals became in contact with a more primitive melt and started developing reverse zoning. **B**. Evolution of seismicity at Ambrym in the period 14 to 20 of December (activity prior to 14 December is minimal), adapted from Shreve et al., (2019). **C**. Evolution of seismicity as a function of distance from Marum, with earthquakes coloured by depth, adapted from Shreve et al., (2019)*

Ascent rates

Volatile diffusion modelling was performed to match the measured H_2O and S concentration profiles (obtained by SIMS) along three melt embayments from the intra-caldera and one from the submarine eruption. All embayments are from melt compositions close to the basaltic end member (i.e. main Marum and Benbow magma). Best fit solutions of the diffusion models are shown in Fig. 9 with initial conditions, model parameters and results given in Table S8. For each embayment we report the results of two type of models: one considering diffusion of the specie of interest only, the other considering diffusion of both species and minimizing error on the fit for both species simultaneously. In all cases, best fit of S profiles only, always result in lower decompression rate estimates (from 0.01 to 0.6 MPa/s) than best fit of H_2O profiles (from 0.39 to 2.7 MPa/s). Embayment PG11 and AF2 show H_2O and S profiles that can be fitted well simultaneously (Fig. 9), yielding decompression rates of 2.3 and 2.7 MPa/s respectively. These two embayments are also the ones recording decompression from highest initial pressure (115 and 68 MPa respectively). Embayments AD5 and AE38 show significant discrepancy between modelled and measured profiles when trying to fit both species simultaneously. These two embayments record decompressions from lower pressures (34 and 37 MPa respectively). A probable explanation is that PG11 and AF2 record direct magma ascent to the surface (from ~4 and ~2.5 km depth respectively) while AD5 and AE38 might have experienced a more complex decompression path, only partially equilibrating at ~1 km depth prior to ascent or ascending in discrete steps. We consider that our best estimates of magma ascent rates during the intra-caldera and submarine eruptions are hence given by the simultaneous modelling of H_2O and S diffusion profiles in embayments AF2 and PG11 respectively, giving ascent rates of 340 and 290 km/h (95 and 80 m/s) respectively. This corresponds to magma travel times of about 30 seconds from ~2.5 km depth to the surface during the intra-caldera eruption and of 1 minute from ~4 km depth to the surface during the submarine eruption. These ascent rates are

506 extremely high. They are, by far the fastest estimates based on the volatile diffusion in
507 embayment method to date (see compilation in Moussallam et al. 2019) and are comparable to
508 estimates based on bubble number density for the andesitic 1997 Soufriere Hills eruption (12-
509 260 m/s; Giachetti et al. 2010) and basaltic-andesite 1986 Izu-Oshima (60-160 m/s; Toramaru
510 2006) eruptions.
511
512 An estimated 13x10^6 m^3 of basaltic magma was degassed during the intra-caldera eruption in
513 about a day (Shreve et al. 2019) making it a magnitude 3.6 eruption with a log10 mass eruption
514 rate (MER) of 5.6. The amount of material erupted during the submarine eruption is unknown.
515 If we consider the volume of magma in the lateral dike (419 to 532 x $10^{\wedge 6} m^3$, Shreve et al.
516 2019) as representative for an eruption period of two days the submarine eruption would be of
517 magnitude 5.2 with a log10 MER of 7 (but note that the base assumption here is not verifiable
518 and these values should not be quoted). The point is that decompression rates of 2.7 and 2.3
519 MPa/s obtained for the intra-caldera and submarine eruptions respectively are much higher
520 than those obtained for eruptions of comparable magnitude using the same technique (see Fig.
521 13 in Moussallam et al. 2019). Whether these fast ascent rates are exceptional for basaltic
522 magmas will only become apparent as more eruptions are studied but to date they are by far
523 the highest.
524
525 From a simple mass conservation argument, the mass eruption rate and ascent velocity can be
526 used to estimate the conduit radius using:
527 $M = \pi r^2 \rho u$ (1)
528 where M is mass eruption rate (in kg/s), r is the conduit radius (in m), ρ is the magma density
529 in ($kg.m^{-3}$) and u is the velocity in ($m.s^{-1}$). This would yield a conduit radius of about 1m for

530 the intra-caldera and 4m for the submarine eruption but we note that such an approach is over-
531 simplistic as the ascent rate is not a constant and should be much higher at the surface than the
532 average value calculated from the embayment technique (which assumes a constant
533 decompression rate) and the eruption (at least the intra-caldera one) occurred along fissures
534 and not a circular vent.
535

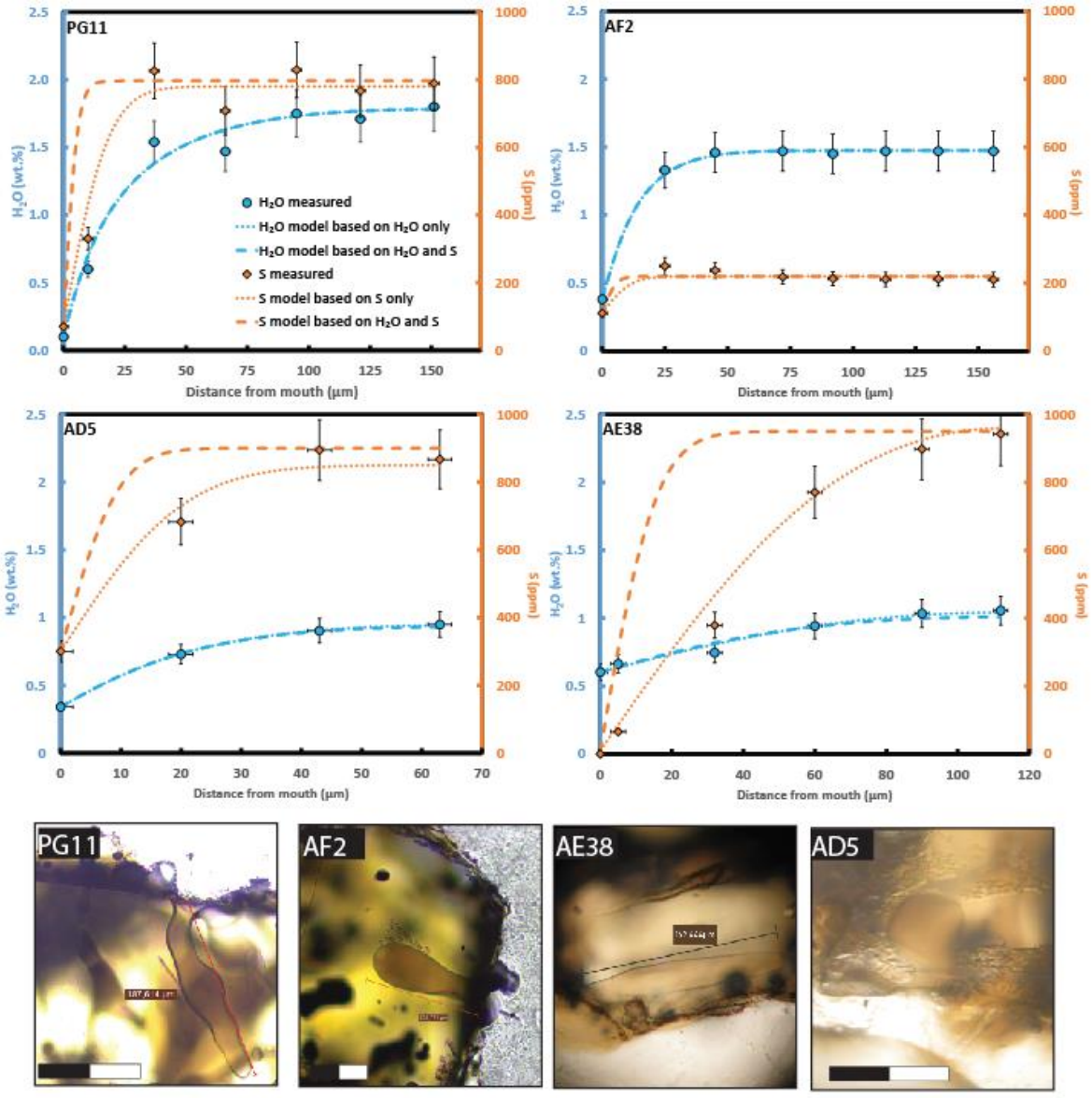

536

537 ***Fig. 9*** *Results of diffusion modelling compared to concentrations (measured by SIMS) for H_2O*
538 *and S in three melt embayments from the intra-caldera and one (PG11) from the submarine*
539 *eruption of Ambrym. Best fit results are shown for two type of models, one (dotted lines)*
540 *considering diffusion of the specie of interest only, the other (dashed lines) considering*

diffusion of both species hence minimizing error on the fit for both species simultaneously. Lower row show microphotograph of each embayment, scale bar represents 100 µm length

DISCUSSION

The Ambrym plumbing system

The crystals and melt inclusions erupted during the 2018 eruption paint a new picture of the plumbing system feeding Ambrym volcano. It is clear from this study and previous work on recent deposits (Firth et al. 2016; Allard et al. 2016a; Sheehan and Barclay 2016) that the main magmatic system underneath Marum and Benbow is of basaltic to basaltic-trachy-andesite composition. Our results, together with previous melt inclusion studies (Allard et al. 2016a) all point to this main magmatic system being vertically extensive, with no clear depth horizon of magma repose/accumulation (Fig. 10). Taking into account the clinopyroxene barometry results of Firth et al. (2016) and Sheehan and Barclay (2016), this vertical magma system might extend to at least 14 km depth, although only the shallowest part of this system was involved in the 2018 eruption. Evidence for this shallow plumbing system reaching up to the surface is provided by the very shallow entrapment pressures of a significant number of melt inclusions, as well as the presence of degassed magma batches, present as a microlite-rich mingled component in the scoriae. The presence of degassed magma is typical of open conduit magmatic systems (e.g., Lautze and Houghton 2005; Gurioli et al. 2014), and evidence of magma convection in the conduits below lava lakes (e.g., Kazahaya et al. 1994; Moussallam et al. 2015b), as was probably the case prior to the 2018 eruption.

The additional information carried in the 2018 eruption deposits is the clear identification of a second magmatic branch, of trachy-andesitic to trachy-dacitic composition. This branch also appears vertically extensive (Fig. 10). We hypothesise that it must be located underneath the Lewolembwi crater as magma of the same composition make up the Tuff ring forming this

crater and a lava flow directly north of it that was emplaced in 1986 (Robin et al. 1991; Picard et al. 1994), as already proposed by Picard et al. (1994). This magmatic batch possibly extends down to 7 km, but not as deep as the main mafic magmatic branch.

The primitive and evolved magmatic branches are clearly chemically related (Fig.3 and Fig.4). We hypothesise that the evolved, trachy-andesitic to trachy-dacitic magma was previously linked at depth to the same parental source as the more primitive trachy-basaltic magma but that this eastern branch was cut-out from the main magmatic channel and started to differentiate in isolation, generating the Lewolembwi and 1986 deposits and being remobilized during the 2018 eruption (see next section).

Interactions between the main (trachy-basaltic) and peripheral (trachy-andesitic to trachy-dacitic) magma chambers must have also occurred prior to the 2018 eruption as evidenced by the presence of diffusion profiles in some olivines that record timescales in the order of years at the very minimum (i.e. could be decades or hundreds of years the profiles were not complete enough to calculate diffusion timescales). Trace element variations also suggest that chemical mixing might have played a role in the resulting compositions and the presence of frequent oscillatory zoning within the clinopyroxene phenocrysts might be further evidence of episodic mafic input into the more evolved magmatic reservoir. How much episodic chemical mixing has occurred between these two components over the years is unknow. Also unknow is how much such interactions have contributed to past eruptions at Ambrym.

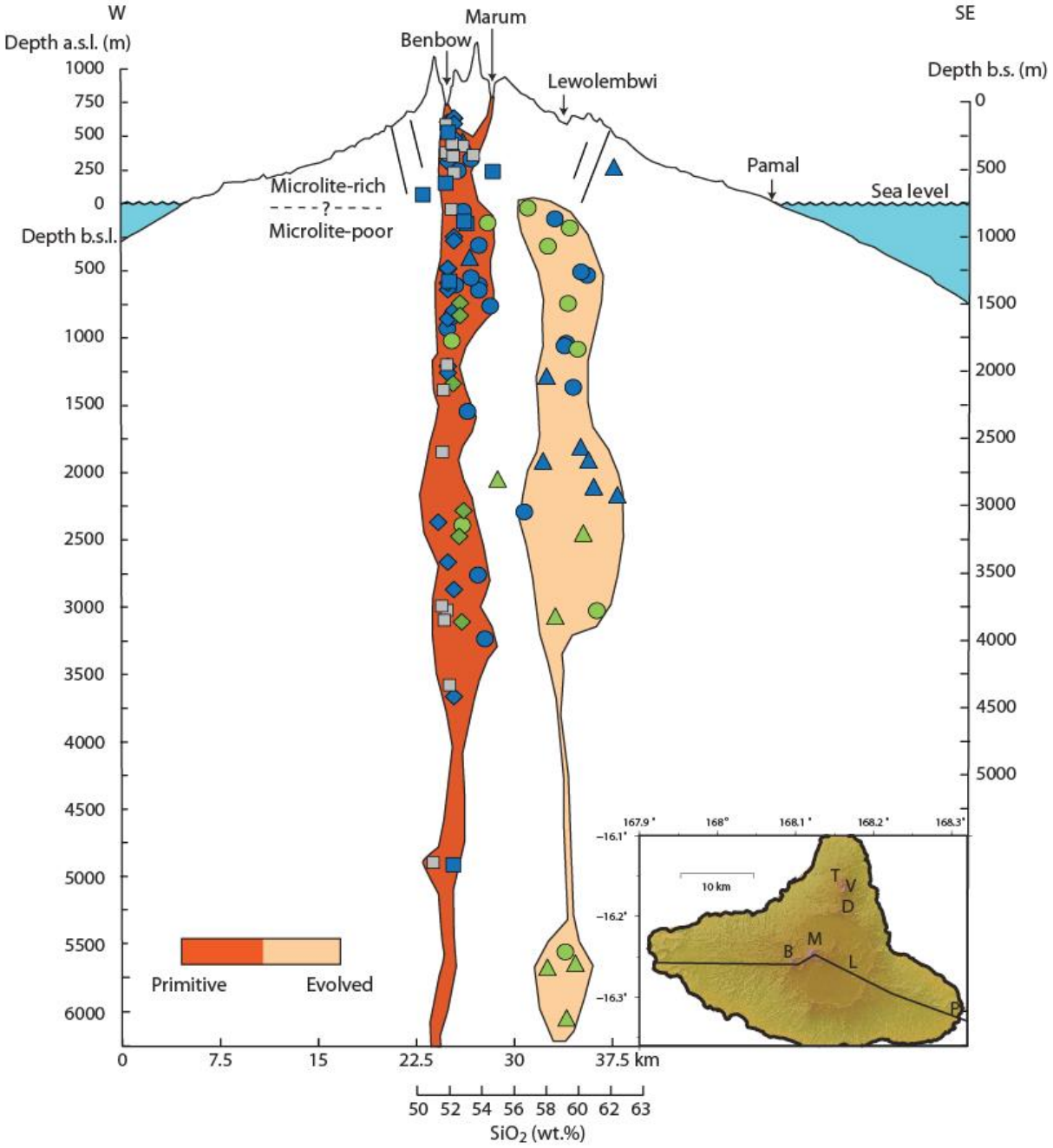

589

590 ***Fig. 10*** *Schematic cross-section representing the Ambrym plumbing system on which melt*
591 *inclusions entrapment pressure and SiO_2 content are superimposed (with no implied relation*
592 *between SiO_2 content and horizontal coordinates of the melt). Inset DEM shows the location*
593 *of the in-land part of the transect used to draw the elevation profile. The more mafic (dark*
594 *orange) and more silicic (light beige) magma chambers are drawn conceptually, their vertical*
595 *extent is constrained by MI entrapment pressures and pyroxene barometry, but their horizontal*
596 *extent is unconstrained. We hypothesise that the more mafic magma is located underneath the*
597 *Benbow and Marum crater as this is the composition that has feed all known eruptive activity*
598 *at these craters while we envision that the more silicic magma is located underneath the*
599 *Lewolembwi crater as magma of the same composition as our evolved end-member, make up*
600 *the Tuff ring forming this crater and the 1986 flow directly north of it* (Robin et al. 1991;
601 Picard et al. 1994). *The upper, degassed part of the mafic system is composed of microlite-rich*

magma, while the deeper part of the system is microlite-poor, the exact depth level separating the two is unconstrained

Triggers and timing of the 2018 Ambrym eruption

Evidence of magma mingling during the 2018 Ambrym eruption are extremely clear, both in the intra-caldera and in the submarine eruptions. Magma mingling can be seen at the micron to millimetre scale in both deposits (Fig. 2). Chemical mixing is evidenced mostly in the composition of the matrix glasses marginally bridging the trachy-basaltic and trachy-andesitic to trachy-dacitic end member compositions (keeping in mind that these could partially also be reflecting mingling at a very small scale) while the melt inclusion compositions mostly record these two end members but show a clear compositional gap in between at SiO_2 contents between ~55 and ~57 wt.% (Fig. 3). These evidence all suggest, to a first order, that encounter of the two magmas occurred for a relatively short time prior to eruption given that mingling textures are preserved and chemical mixing between the two end members is incomplete. This is confirmed quantitatively by the modelling of diffusion profiles in olivine crystals from the evolved components brought in contact with the more mafic component at calculated timescales of hours to a few days prior to eruption. While it is clear that the encounter of these two magmas played an important part in this eruption the real "trigger" is the event that brought the main branch of the plumbing system (trachy-basalt) in contact with the previously isolated and more differentiated eastern branch (trachy-andesite to trachy-dacite). In the following discussion we combine our petrological findings with visual and geophysical observations to constrain the nature and timing of the processes that occurred during the 2018 eruption.

1. An over pressurizing magmatic system

In the two weeks directly preceding the eruption the height of the main lava lake at Marum crater increased rapidly with a rise in the lake level of ~60 m between 30 November and 14

December 2018 (Fig. S1). This increase in lake level likely indicates increased pressurization of the magmatic system around that time.

2. First diking event, magma mixing, lava lake drainage and intra-caldera eruption.

Fe-Mg and Mn diffusion modelling from an olivine crystal erupted between 14 December at 23:20 and 15 December at 00:01 UTC at Lewolembwi crater records diffusion timescales < 10h, indicating than magma mixing was initiated within 10h of eruption (i.e. in the afternoon of the 14 December 2018). This should be taken as an order of magnitude estimate being based on a single diffusion profile. Geodetic modelling by Shreve et al., (2019) based on inversion of InSAR interferogram for images covering the November 3 to December 15, 00:24 interval identified the emplacement of a shallow dike with 2 m maximum opening (Fig.11). While the exact timing of this dike emplacement cannot be resolved by InSAR, we suggest that this dyking event likely put in contact the two previously disconnected branches of the Ambrym plumbing system with primitive magma from the main branch intersecting evolved magma from the eastern branch and rising together to erupt at the surface. The intersection of the two magma bodies probably occurred at shallow, 1 to 2.5 km depth (according to dike geodetic modelling), draining the top 1 km portion of the main magmatic branch (as evidenced by the abundance of magma from the top 1km in the intra-caldera eruption and lack of any such magma in the subsequent submarine eruption) (Fig. 11), causing the disappearance of the five lava lakes and partial collapse of the Marum and Benbow craters. Magma ascent from ~2.5 km depth to the surface took less than 1 minute for magma ascending directly but was slower for magma experiencing more complex history such as descending and laterally migrating prior to eruption.

3. Second diking event, magma migration and submarine eruption.

Fe-Mg, Mn, Ni and Ca diffusion modelling from three olivine crystals erupted during the submarine eruption are all consistent with diffusion timescales <2 days. The estimated start of the submarine eruption is at 16:00 on 17 December, based on abrupt decrease of seismic moment release (Shreve et al., 2019). Magma mixing was therefore initiated sometime between the 15 December evening and the 17 December (Fig. 7). This corresponds to a period of intense seismic activity and surface deformation starting with a Mw 5.6 strike-slip earthquake on 15 December at 20h21 and interpreted from geodetic modelling as the lateral, eastward propagation of a dike with ~3 m of opening along >30 km distance (Fig. 11) (Shreve et al., based on inversion of InSAR interferogram for images covering the 15 to 18 December period). Magma mixing and dike propagation are therefore synchronous, and it seems likely that both magma type became entrained in the same dike where mixing occurred. The tip of the dike however was likely composed solely of the "main branch", more primitive magma as the very first scoria that reached the island shore showed no indication of mixing and are all of basaltic trachy-andesite to basaltic-andesite composition (Fig. 3). One caveat to consider however is that while the start date of the submarine eruption is well estimated, we do not have an exact date or time on the moment at which our scoria samples were erupted. The eruption might have continued for up to two months (Shreve et al., 2019). Our diffusion timescales might hence not be directly comparable to seismic events preceding the eruption initiation, but they still indicate timescales of magma mixing with <2 days of mixing prior to eruption. While lateral magma transport might have taken up to two days, vertical ascent from ~4 km to the submarine eruption site took just a minute, ascending at an average speed of ~80 km/h.

675

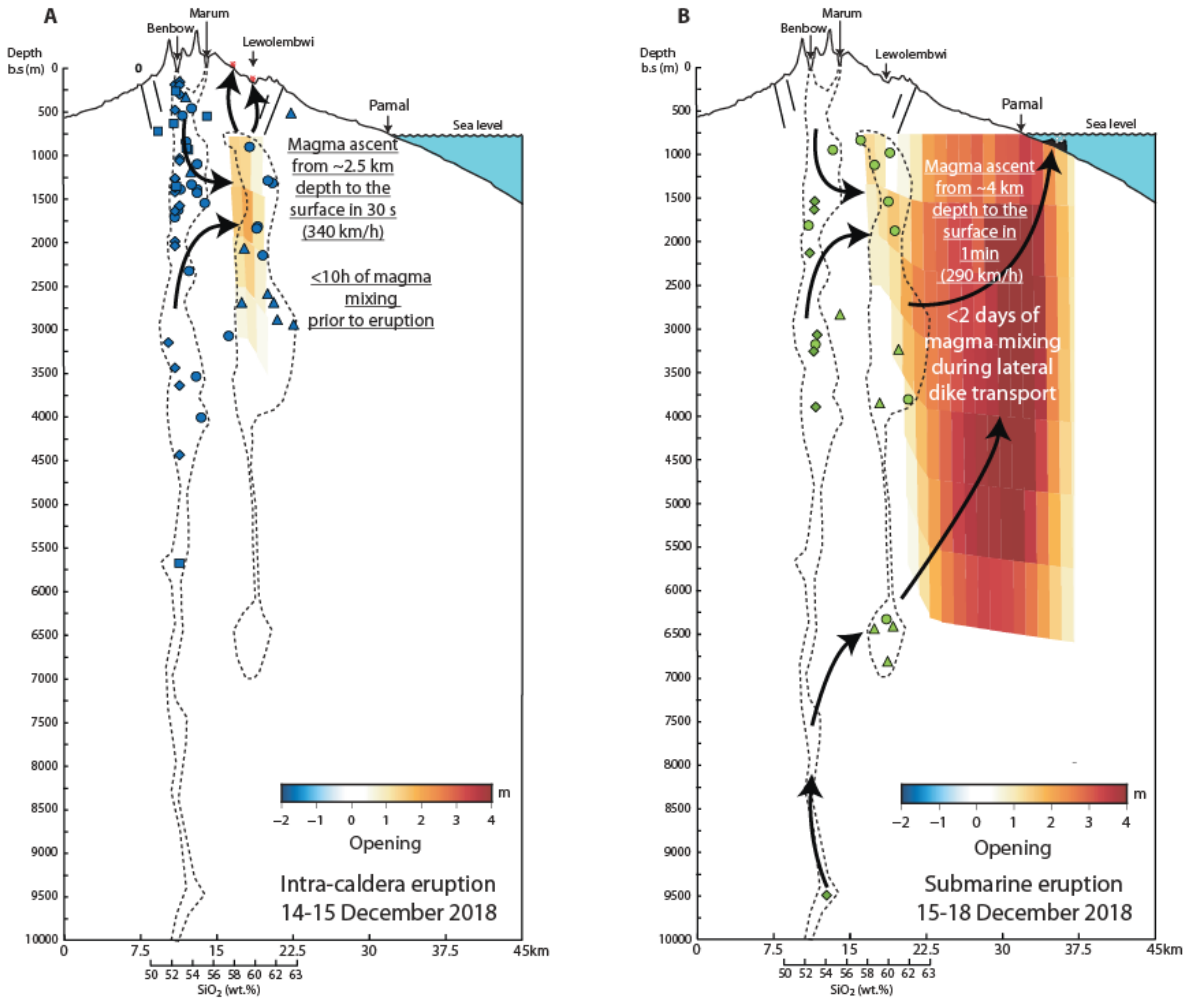

676

677 ***Fig. 11*** *Schematic cross-section of Ambrym volcano comparing the entrapment pressure of*
678 *melt inclusions erupted during (**A**) the intra-caldera eruption and (**B**) the submarine eruption*
679 *with the depth of diking events in the period (**A**) November 3 to December 15 at 00:24 and (**B**)*
680 *December 15 to 18 (geodetic models from Shreve et al., 2019). Dotted lines represent the*
681 *hypothesized locations of the primitive and evolved magmatic branches (see Fig. 10 caption*
682 *and text for details). Black arrows show the inferred directions of magma migration. In (**A**) the*
683 *upper ~1km of the main magmatic branch underneath Benbow and Marum is drained, mixes*
684 *with the eastern, evolved magmatic branch and erupted together at Lewolembwi (the*
685 *composition of the lava erupted synchronously between Lewolembwi and Marum is unknown).*
686 *In (**B**) eastward magma migration might originate, or at least has a contribution from deeper*
687 *levels. Timescales of magma mixing and ascent rate from diffusion modelling of reverse*
688 *compositional zoning in olivine and volatile in melt embayments are reported for each eruption*
689

690

691 **Comparison with other lava-lake-draining rift eruptions**

692 If we look in detail at the last three eruptions that terminated or partially drained lava lakes at
693 basaltic volcanoes along a rift axis (2017-2020 Erta 'Ale, 2018 Kīlauea and 2018 Ambrym),
694 clear patterns seem to emerge. First, they all seem to be preceded by high levels of their lava
695 lake. At Kīlauea, the 2018 eruption was preceded by a high level of the lava lake at the summit
696 crater and a rising lava pond at Pu‘u ‘Ō‘ō (Neal et al. 2019). At Erta ‘Ale the lake level had
697 been rising (yet not constantly) since 2000 (Barnie et al. 2016), overflowing its bank directly
698 prior to the 2017 fissure eruption (Global Volcanism Program, 2017). As seen previously, at
699 Ambrym the lake level rose rapidly in the weeks prior to eruption (Fig. S1). Another, older
700 example is the 1977 lake-draining fissure eruption of Nyiragongo Volcano, which was
701 preceded by a rise in the lake level of 200 m from 1959 to 1976 (Tazieff 1977). An inescapable
702 conclusion seems to be that pressure build up in the magmatic system (as tracked by rising lava
703 lake level), always precedes this type of eruption.

704

705 In all these examples, lake drainage (or subsidence) is then synchronous with magma migration
706 and lateral fissure eruptions (Tazieff 1977; Moore et al. 2019; Neal et al. 2019; Shreve et al.
707 2019). This phenomenon was (to our knowledge) first documented at Kīlauea volcano in 1924
708 where drainage of the hundred-year-long lava lake accompanied an intrusion in the eastern rift
709 zone (Jaggar and Finch 1924) and has since been documented extensively at Kīlauea (see
710 review by Patrick et al. 2019). Yet another example is the 1913 eruption of Ambrym which
711 had a remarkably similar pattern to the 2018 eruption. In 1913, the eruption began with a fissure
712 eruption inside the caldera followed by magma migration along the rift axis (to the west) and
713 magma eruption near the shoreline (Németh and Cronin 2011). Although it is not known how
714 the lava lake level responded at that time, Németh and Cronin (2008)’s investigation of

Marum's crater walls revealed that episodes of lava lake pounding and subsequent drainage to feed flank eruptions and excavation of the crater by associated phreatic to phreatomagmatic eruptions has been a common occurrence throughout the volcano's history. Lake drainage through dike migration and flank eruption is hence probably as recurrent a phenomenon at Ambrym as it is at Kīlauea.

A peculiarity of the 2018 Ambrym eruption is the extrusion of evolved lava together with lava of the same composition as the lava lakes. As seen in the previous section, it appears that a dike propagating from the main magmatic branch intersected and remobilised evolved magma from a peripheric magma chamber. Interestingly the same phenomenon seems to have occur during the 2018 Kīlauea eruption during which an evolved (andesitic) peripheral magmatic pocket was intersected by the main dike and remobilised during the eruption (although in the Kīlauea case this occurred significantly further down-rift from the main system, Gansecki et al. 2019). The presence of such isolated, differentiated and still eruptible magmatic branches at the periphery of main magmatic systems might therefore be a more common occurrence than previously realised.

CONCLUSIONS

The 2018 Ambrym eruption, whilst volumetrically mostly occurring underground, was spectacular. It drained five active lava lakes, caused partial collapse of their crater accompanied with large, possibly phreatic, explosions, a 2 m subsidence of the 12 km diameter caldera, magma migration for 30 km horizontal distance and eruption of mingled and slightly chemically mixed magma at intra-caldera fissure eruptions and just off the SE coast as a shallow submarine eruption. Much like previous ones, this eruption highlighted the fact that whilst most population centres on Ambrym island are located at large distance from the main vents, those located along the rift axis will continue to be at risk and impacted by future eruptive events as magma migrates quickly to the shoreline. In this contribution we presented the results of major and volatile element analyses in bulk rocks, matrix glasses, melt inclusions, embayments, and minerals to shed light on the nature and timing of magmatic processes operating during this eruption. The main conclusions we draw from our findings are (1) The eruption began with the meeting, mingling and limited chemical mixing of trachy-basaltic magma from the main magmatic system with more evolved trachy-andesitic to trachy-dacitic magma from an older peripheral and previously cut-off branch. (2) In detail, the trachy-basaltic magma is itself composed of two mingled component, one microlite-poor and one microlite-rich, the second possibly reflecting degassing processes due to convection at shallow depth underneath the lava lakes. (3) The primitive and evolved magmatic branches interact periodically, with at least one interaction occurring more than a year prior to the 2018 eruption. (4) Magma mixing took place less than 10h prior to intra-caldera eruption and for about 2 days during magma transport in a >30 km dike from the centre of the island to the coast prior to submarine eruption. Magma ascent from 2.5 and 4 km depth to the surface took place at rates in the order of 95±24 to 80±6 m/s. (5) Comparison with other lava-lake-draining eruptions reveals that lake level rise – indicating pressurisation of the magmatic system – always

precedes this type of eruption, highlighting the usefulness of this parameter for future monitoring. Furthermore, the presence of peripheral, more evolved magma pockets, cut-off from the main magmatic system but still mobilizable and eruptible could be a more common occurrence than previously realised.

REFERENCES

Allard P, Aiuppa A, Bani P, et al (2016a) Prodigious emission rates and magma degassing budget of major, trace and radioactive volatile species from Ambrym basaltic volcano, Vanuatu island Arc. J Volcanol Geotherm Res 322:119–143. https://doi.org/10.1016/j.jvolgeores.2015.10.004

Allard P, Burton M, Sawyer G, Bani P (2016b) Degassing dynamics of basaltic lava lake at a top-ranking volatile emitter: Ambrym volcano, Vanuatu arc. Earth Planet Sci Lett 448:69–80. https://doi.org/10.1016/j.epsl.2016.05.014

Anderson AT, Brown GG (1993) CO_2 contents and formation pressures of some Kilauean melt inclusions. Am Mineral 78:794–803

Barnie TD, Oppenheimer C, Pagli C (2016) Does the lava lake of Erta 'Ale volcano respond to regional magmatic and tectonic events? An investigation using Earth Observation data. Geol Soc Lond Spec Publ 420:181–208. https://doi.org/10.1144/SP420.15

Bouvier A-S, Métrich N, Deloule E (2008) Slab-Derived Fluids in the Magma Sources of St. Vincent (Lesser Antilles Arc): Volatile and Light Element Imprints. J Petrol 49:1427–1448. https://doi.org/10.1093/petrology/egn031

Burgi P-Y, Darrah TH, Tedesco D, Eymold WK (2014) Dynamics of the Mount Nyiragongo lava lake. J Geophys Res Solid Earth 119:2013JB010895. https://doi.org/10.1002/2013JB010895

Carn SA, Fioletov VE, McLinden CA, et al (2017) A decade of global volcanic SO2 emissions measured from space. Sci Rep 7:44095. https://doi.org/10.1038/srep44095

Chen Y, Provost A, Schiano P, Cluzel N (2011) The rate of water loss from olivine-hosted melt inclusions. Contrib Mineral Petrol 162:625–636. https://doi.org/10.1007/s00410-011-0616-5

Danyushevsky LV (2001) The effect of small amounts of H2O on crystallisation of mid-ocean ridge and backarc basin magmas. J Volcanol Geotherm Res 110:265–280. https://doi.org/10.1016/S0377-0273(01)00213-X

Danyushevsky LV, Plechov P (2011) Petrolog3: Integrated software for modeling crystallization processes. Geochem Geophys Geosystems 12:n/a-n/a. https://doi.org/10.1029/2011GC003516

790 Ferguson DJ, Gonnermann HM, Ruprecht P, et al (2016) Magma decompression rates during
791 explosive eruptions of Kīlauea volcano, Hawaii, recorded by melt embayments. Bull
792 Volcanol 78:71. https://doi.org/10.1007/s00445-016-1064-x

793 Firth C, Handley H, Turner S, et al (2016) Variable Conditions of Magma Storage and
794 Differentiation with Links to Eruption Style at Ambrym Volcano, Vanuatu. J Petrol
795 57:1049–1072. https://doi.org/10.1093/petrology/egw029

796 Gansecki C, Lee RL, Shea T, et al (2019) The tangled tale of Kīlauea's 2018 eruption as told
797 by geochemical monitoring. Science 366:. https://doi.org/10.1126/science.aaz0147

798 Giachetti T, Druitt TH, Burgisser A, et al (2010) Bubble nucleation, growth and coalescence
799 during the 1997 Vulcanian explosions of Soufrière Hills Volcano, Montserrat. J
800 Volcanol Geotherm Res 193:215–231.
801 https://doi.org/10.1016/j.jvolgeores.2010.04.001

802 Girona T, Costa F (2013) DIPRA: A user-friendly program to model multi-element diffusion
803 in olivine with applications to timescales of magmatic processes. Geochem Geophys
804 Geosystems 14:422–431. https://doi.org/10.1029/2012GC004427

805 Gorton MP (1977) The geochemistry and origin of quaternary volcanism in the New Hebrides.
806 Geochim Cosmochim Acta 41:1257–1270. https://doi.org/10.1016/0016-
807 7037(77)90071-0

808 Gurioli L, Colo' L, Bollasina AJ, et al (2014) Dynamics of Strombolian explosions: Inferences
809 from field and laboratory studies of erupted bombs from Stromboli volcano. J Geophys
810 Res Solid Earth 119:319–345. https://doi.org/10.1002/2013JB010355

811 Harris AJL (2008) Modeling lava lake heat loss, rheology, and convection. Geophys Res Lett
812 35:. https://doi.org/10.1029/2008GL033190

813 Harris AJL, Carniel R, Jones J (2005) Identification of variable convective regimes at Erta Ale
814 Lava Lake. J Volcanol Geotherm Res 142:207–223.
815 https://doi.org/10.1016/j.jvolgeores.2004.11.011

816 Hauri E, Wang J, Dixon JE, et al (2002) SIMS analysis of volatiles in silicate glasses: 1.
817 Calibration, matrix effects and comparisons with FTIR. Chem Geol 183:99–114.
818 https://doi.org/10.1016/S0009-2541(01)00375-8

819 Iacono-Marziano G, Morizet Y, Le Trong E, Gaillard F (2012) New experimental data and
820 semi-empirical parameterization of H2O–CO2 solubility in mafic melts. Geochim
821 Cosmochim Acta 97:1–23. https://doi.org/10.1016/j.gca.2012.08.035

822 Jaggar TA, Finch RH (1924) The explosive eruption of Kilauea in Hawaii, 1924. Am J Sci
823 Series 5 Vol. 8:353–374. https://doi.org/10.2475/ajs.s5-8.47.353

824 Kazahaya K, Shinohara H, Saito G (1994) Excessive degassing of Izu-Oshima volcano: magma
825 convection in a conduit. Bull Volcanol 56:207–216.
826 https://doi.org/10.1007/BF00279605

827 Kress VC, Carmichael ISE (1988) Stoichiometry of the iron oxidation reaction in silicate melts.
828 Am Mineral 73:1267–1274

829 Lange RL, Carmichael ISE (1990) Thermodynamic properties of silicate liquids with emphasis
830 on density, thermal expansion and compressibility. Rev Mineral Geochem 24:25–64

831 Lautze NC, Houghton BF (2005) Physical mingling of magma and complex eruption dynamics
832 in the shallow conduit at Stromboli volcano, Italy. Geology 33:425–428.
833 https://doi.org/10.1130/G21325.1

834 Moore C, Wright T, Hooper A, Biggs J (2019) The 2017 Eruption of Erta 'Ale Volcano,
835 Ethiopia: Insights Into the Shallow Axial Plumbing System of an Incipient Mid-Ocean
836 Ridge. Geochem Geophys Geosystems 20:5727–5743.
837 https://doi.org/10.1029/2019GC008692

838 Moussallam Y, Bani P, Curtis A, et al (2016) Sustaining persistent lava lakes: Observations
839 from high-resolution gas measurements at Villarrica volcano, Chile. Earth Planet Sci
840 Lett 454:237–247. https://doi.org/10.1016/j.epsl.2016.09.012

841 Moussallam Y, Oppenheimer C, Scaillet B, et al (2015a) Megacrystals track magma convection
842 between reservoir and surface. Earth Planet Sci Lett 413:1–12.
843 https://doi.org/10.1016/j.epsl.2014.12.022

844 Moussallam Y, Oppenheimer C, Scaillet B, et al (2015b) Megacrystals track magma
845 convection between reservoir and surface. Earth Planet Sci Lett 413:1–12.
846 https://doi.org/10.1016/j.epsl.2014.12.022

847 Moussallam Y, Rose-Koga EF, Koga KT, et al (2019) Fast ascent rate during the 2017–2018
848 Plinian eruption of Ambae (Aoba) volcano: a petrological investigation. Contrib
849 Mineral Petrol 174:90. https://doi.org/10.1007/s00410-019-1625-z

850 Neal CA, Brantley SR, Antolik L, et al (2019) The 2018 rift eruption and summit collapse of
851 Kīlauea Volcano. Science 363:367–374. https://doi.org/10.1126/science.aav7046

852 Németh K, Cronin SJ (2011) Drivers of explosivity and elevated hazard in basaltic fissure
853 eruptions: The 1913 eruption of Ambrym Volcano, Vanuatu (SW-Pacific). J Volcanol
854 Geotherm Res 201:194–209. https://doi.org/10.1016/j.jvolgeores.2010.12.007

855 Németh K, Cronin SJ (2008) Volcanic craters, pit craters and high-level magma-feeding
856 systems of a mafic island-arc volcano: Ambrym, Vanuatu, South Pacific. Geol Soc
857 Lond Spec Publ 302:87–102. https://doi.org/10.1144/SP302.6

858 Oppenheimer C, Lomakina AS, Kyle PR, et al (2009) Pulsatory magma supply to a phonolite
859 lava lake. Earth Planet Sci Lett 284:392–398

860 Patrick M, Swanson D, Orr T (2019) A review of controls on lava lake level: insights from
861 Halema'uma'u Crater, Kīlauea Volcano. Bull Volcanol 81:13.
862 https://doi.org/10.1007/s00445-019-1268-y

863 Picard C, Monzier M, Eissen J-P, Robin C (1994) Concomitant evolution of tectonic
864 environment and magma geochemistry, Ambrym volcano (Vanuatu, New Hebrides
865 arc). Geol Soc Lond Spec Publ 81:135–154.
866 https://doi.org/10.1144/GSL.SP.1994.081.01.08

867 Pichavant M, Carlo ID, Rotolo SG, et al (2013) Generation of CO2-rich melts during basalt
868 magma ascent and degassing. Contrib Mineral Petrol 166:545–561.
869 https://doi.org/10.1007/s00410-013-0890-5

870 Robin C, Monzier M, Eissen J-P, et al (1991) Coexistence de lignées HK et MK dans les
871 pyroclastites associées à la caldera d'Ambrym (Vanuatu - Arc des Nouvelles-
872 Hébrides). Comptes Rendus Académie Sci 2 Mécanique 313:1425–1432

873 Rose-Koga EF, Koga KT, Devidal J-L, et al (2020) In-situ measurements of magmatic volatile
874 elements, F, S, and Cl, by electron microprobe, secondary ion mass spectrometry, and
875 heavy ion elastic recoil detection analysis. Am Mineral 105:616–626.
876 https://doi.org/10.2138/am-2020-7221

877 Rose-Koga EF, Koga KT, Hamada M, et al (2014) Volatile (F and Cl) concentrations in Iwate
878 olivine-hosted melt inclusions indicating low-temperature subduction. Earth Planets
879 Space 66:81. https://doi.org/10.1186/1880-5981-66-81

880 Schiano P, Monzier M, Eissen J-P, et al (2010) Simple mixing as the major control of the
881 evolution of volcanic suites in the Ecuadorian Andes. Contrib Mineral Petrol 160:297–
882 312. https://doi.org/10.1007/s00410-009-0478-2

883 Sheehan F, Barclay J (2016) Staged storage and magma convection at Ambrym volcano,
884 Vanuatu. J Volcanol Geotherm Res 322:144–157.
885 https://doi.org/10.1016/j.jvolgeores.2016.02.024

886 Shimizu K, Shimizu N, Komiya T, et al (2009) CO2-rich komatiitic melt inclusions in Cr-
887 spinels within beach sand from Gorgona Island, Colombia. Earth Planet Sci Lett
888 288:33–43. https://doi.org/10.1016/j.epsl.2009.09.005

889 Shishkina TA, Botcharnikov RE, Holtz F, et al (2014) Compositional and pressure effects on
890 the solubility of H2O and CO2 in mafic melts. Chem Geol 388:112–129.
891 https://doi.org/10.1016/j.chemgeo.2014.09.001

892 Shreve T, Grandin R, Boichu M, et al (2019) From prodigious volcanic degassing to caldera
893 subsidence and quiescence at Ambrym (Vanuatu): the influence of regional tectonics.
894 Sci Rep 9:1–13. https://doi.org/10.1038/s41598-019-55141-7

895 Smythe DJ, Wood BJ, Kiseeva ES (2017) The S content of silicate melts at sulfide saturation:
896 New experiments and a model incorporating the effects of sulfide composition. Am
897 Mineral 102:795–803. https://doi.org/10.2138/am-2017-5800CCBY

898 Tazieff H (1977) An exceptional eruption: Mt. Niragongo, Jan. 10th, 1977. Bull Volcanol
899 40:189–200. https://doi.org/10.1007/BF02596999

900 Tazieff H (1994) Permanent lava lakes: observed facts and induced mechanisms. J Volcanol
901 Geotherm Res 63:3–11. https://doi.org/10.1016/0377-0273(94)90015-9

902 Toplis MJ (2005) The thermodynamics of iron and magnesium partitioning between olivine
903 and liquid: criteria for assessing and predicting equilibrium in natural and experimental
904 systems. Contrib Mineral Petrol 149:22–39. https://doi.org/10.1007/s00410-004-0629-
905 4

Toramaru A (2006) BND (bubble number density) decompression rate meter for explosive volcanic eruptions. J Volcanol Geotherm Res 154:303–316. https://doi.org/10.1016/j.jvolgeores.2006.03.027

Witham F, Llewellin EW (2006) Stability of lava lakes. J Volcanol Geotherm Res 158:321–332. https://doi.org/10.1016/j.jvolgeores.2006.07.004

ACKNOWLEDGEMENTS

This research was conducted as part of the Trail by Fire II – Closing the Ring project (PI: Y. Moussallam) with support from National Geographic (grant number CP-122R-17) the Rolex Awards for Enterprise and the French national Research Institute for Development (IRD). We thank Nordine Bouden and Etienne Deloule of CRPG (France) for their precious guidance during SIMS analysis. We thank Mhammed Benbakkar for ICP-AES analyses and Claire Fonquernie for help with sample preparation. MB acknowledges support from the French National Research Agency (ANR) for funding the VOLCPLUME project (ANR-15-CE04-0003-01). We are grateful for the constructive reviews provided by Nicole Métrich and two anonymous reviewers on an earlier version of this manuscript and to Nicole Métrich for editorial handling.